annual N burden of ≈0.5 kg ha^{-1} deposited primarily during the summer. This burden represents ≈40% of the total N dry deposition and ≈15% of the total atmospheric N input (≈3.5 kg ha^{-1} $year^{-1}$) estimated by similar methods and wet deposition data (*22*) (Table 1). The total N deposition is equivalent to ≥25% of the total N translocated through the roots (12.5 kg ha^{-1} $year^{-1}$) of a similar forest 150 km to the north (*23*) and represents a sizable nutrient input to this N-limited ecosystem.

The total deposition of all N species to Roosevelt National Forest is much less than that in other coniferous forests in the eastern United States and Europe (*24*) (Table 2) and is well below the estimated threshold for forest damage (≈10 to 20 kg ha^{-1} $year^{-1}$) (*25*). Table 2 contrasts the N burdens in forests near sources of high agricultural and low industrial emissions (Roosevelt), low agricultural and high industrial emissions (Oak Ridge, Tennessee), and high agricultural and high industrial emissions (Göttingen, Germany). Forests in areas with high $(SO_2 + NO_x)/NH_3$ emission ratios (for example, Oak Ridge and the eastern United States) may simultaneously act as net sinks for anthropogenic N in the form of NO_x, HNO_3, NO_3^-, and NH_4^+ while emitting gaseous NH_3 to the atmosphere. This results from the presence of unneutralized sulfate aerosols that scavenge NH_3 and depress the ambient NH_3 mixing ratios to well below the compensation point [≤0.05 ppbv (*26, 27*)]. These emissions can account for both the presence of NH_3 in regions with no known anthropogenic sources at mixing ratios greater than predicted from the NH_3-H_2SO_4-NH_4HSO_4-$(NH_4)_2SO_4$ equilibrium and the ubiquity of ammonium sulfate and bisulfate aerosols in the atmosphere (*28*).

REFERENCES AND NOTES

1. G. L. Hutchinson, R. J. Millington, D. B. Peters, *Science* **175**, 771 (1972).
2. O. T. Denmead, J. R. Freney, J. R. Simpson, *Soil Biol. Biochem.* **8**, 161 (1976).
3. V. P. Aneja, H. H. Rogers, E. P. Stahel, *J. Air Pollut. Control Assoc.* **36**, 1338 (1986).
4. L. W. A. Van Hove, A. J. Koops, E. H. Adema, W. J. Vredenber, G. A. Pieters, *Atmos. Environ.* **21**, 1759 (1987).
5. _____, *ibid.* **23**, 1479 (1989).
6. H. H. Rogers and V. P. Aneja, *Environ. Exp. Bot.* **20**, 251 (1980).
7. B. Nihlgård, *Ambio* **14**, 2 (1985).
8. E.-D. Schulze, *Science* **244**, 776 (1989).
9. A. R. McLeod *et al.*, *Nature* **347**, 277 (1990).
10. G. D. Farquhar, P. M. Firth, R. Wetselaar, B. Weir, *Plant Physiol.* **66**, 710 (1980).
11. E. Lemon and R. Van Houtte, *Agron. J.* **72**, 876 (1980).
12. T. R. Sinclair and R. F. Van Houtte, *Agric. Environ.* **7**, 237 (1982).
13. O. T. Denmead, J. R. Freney, J. R. Simpson, *Soil Sci. Soc. Am. J.* **46**, 149 (1982).
14. I. E. Galbally, G. D. Farquhar, G. P. Ayers, in *Cycling of Carbon, Nitrogen, Sulfur, and Phosphorus in Terrestrial and Aquatic Ecosystems*, J. R. Freney and I. E. Galbally, Eds. (Springer-Verlag, Berlin, 1982), pp. 1–9.
15. J. M. Roberts, A. O. Langford, P. D. Goldan, F. C. Fehsenfeld, *J. Atmos. Chem.* **7**, 137 (1988).
16. Simultaneous gaseous NH_3 and filter measurements (*15, 17*) showed the mean concentrations of particulate NH_3, NH_4^+, and SO_4^{2-} at Boulder to be 231, 44, and 17 nmol m^{-3}, respectively. The corresponding concentrations at Niwot Ridge were 15, 14, and 6.5 nmol m^{-3}. These results show that gas-to-particle conversion can be neglected as a sink for NH_3 transported across the forest because particulate SO_4^{2-} was fully neutralized ($[NH_4^+]/[SO_4^{2-}] \geq 2$) at both sites with most of the NH_3 remaining in the gas phase ($[NH_3]/[NH_4^+] \geq 1$). Gaseous HNO_3 and particulate NO_3^- measurements suggest that NH_4NO_3 formed in Boulder will evaporate in transit to Niwot Ridge (*17*). Photochemical destruction is negligible on the time scale of transport (≤8 hours). Finally, only data from dry periods are considered so that cloud and precipitation scavenging can be ignored.
17. A. O. Langford, R. B. Norton, F. C. Fehsenfeld, *Eos* **70**, 1008 (1989).
18. S. M. Dabney and D. R. Bouldin, *Atmos. Environ. Part A* **24**, 2655 (1990).
19. R. M. Wallsgrove, A. J. Keys, P. J. Lea, B. J. Miflin, *Plant Cell Environ.* **6**, 301 (1983).
20. G. F. Dykstra, *Can. J. For. Res.* **4**, 201 (1974).
21. D. D. Parrish *et al.*, *J. Geophys. Res.* **95**, 1817 (1990).
22. National Acid Deposition Program (NADP)/National Trends Network Annual Data Summary, *Precipitation Chemistry in the United States* (Natural Resource Ecology Laboratory, Fort Collins, CO, 1987–1988).
23. T. J. Fahey, J. B. Yavitt, J. A. Pearson, D. H. Knight, *Biogeochemistry* **257**, 257 (1985).
24. S. E. Lindberg, M. Bredmeier, D. A. Schaefer, L. Qi, *Atmos. Environ. Part A* **24**, 2207 (1990).
25. J. Nilsson, Ed., "Critical loads for nitrogen and sulphur" (Nordic Council of Ministers Report 11, Copenhagen, 1986).
26. J. D. Tjepkema, R. J. Cartica, H. F. Hemond, *Nature* **294**, 445 (1981).
27. I. N. Tang, *Atmos. Environ.* **14**, 819 (1980).
28. N.-C. Lau and R. C. Charlson, *ibid.* **11**, 475 (1978).
29. E. J. Williams *et al.*, *Eos* **68**, 1215 (1987).
30. J. H. Duyzer, A. M. H. Bouman, H. S. M. A. Diederen, R. M. van Alst, "Measurements of dry deposition velocities of NH_3 and NH_4^+ over natural terrains" [Netherlands Organization for Applied Scientific Research (TNO) Division of Technology for Society Report 99-02, Delft, 1987].
31. E. J. Williams, personal communication.
32. P. J. Hanson *et al.*, *Atmos. Environ.* **23**, 1783 (1989).
33. A. O. Langford, P. D. Goldan, F. C. Fehsenfeld, *J. Atmos. Chem.* **8**, 359 (1989).

34. This research was funded as part of the National Acid Precipitation Assessment Program by the National Oceanic and Atmospheric Administration.

22 July 1991; accepted 18 November 1991

Topographic and Magnetic-Sensitive Scanning Tunneling Microscope Study of Magnetite

R. WIESENDANGER, I. V. SHVETS,* D. BÜRGLER, G. TARRACH, H. J. GÜNTHERODT, J. M. D. COEY, S. GRÄSER

The topographic and magnetic surface structure of a natural single crystal of magnetite (Fe_3O_4), a common mineral, has been studied from the submicrometer scale down to the atomic scale with a scanning tunneling microscope having nonmagnetic tungsten as well as ferromagnetic iron probe tips. Several different (001) crystal planes were imaged to atomic resolution with both kinds of tips. A selective imaging of the octahedrally coordinated Fe B-sites in the Fe–O planes, and even a selective imaging of the different magnetic ions Fe^{2+} and Fe^{3+}, has been achieved, demonstrating for the first time that magnetic imaging can be realized at the atomic level.

THE SCANNING TUNNELING MICROscope (STM), developed by Binnig, Rohrer, Gerber, and Weibel (*1*), is already well known for its ability to image surface structures of conducting samples down to the atomic scale. The most significant contributions of STM have initially been made in the field of semiconductor surfaces (*2, 3*) and, more recently, in the fields of metal surfaces (*4*), superconductivity (*5*), charge-density wave systems (*6*), and atomic-scale writing (*7*) and switching (*8*). We demonstrate that the STM can also be a

R. Wiesendanger, I. V. Shvets, D. Bürgler, G. Tarrach, H.-J. Güntherodt, University of Basel, Department of Physics, Klingelbergstrasse 82, CH-4056 Basel, Switzerland.
J. M. D. Coey, Trinity College, Department of Pure and Applied Physics, Dublin 2, Ireland.
S. Gräser, University of Basel, Department of Mineralogy, Bernoullistrasse 32, CH-4056 Basel, Switzerland.

*On leave from Trinity College, Department of Pure and Applied Physics, Dublin 2, Ireland.

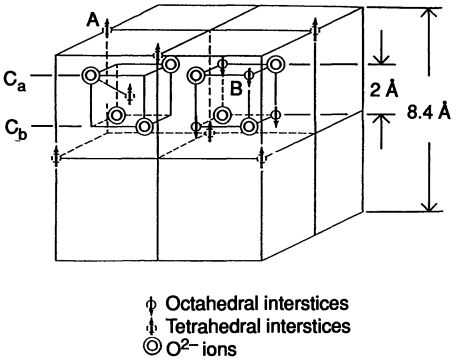

Fig. 1. Simplified picture of the conventional unit cell of magnetite, including its spin structure. There are (001) planes built up by the Fe A-sites, as well as other (001) planes (C_a and C_b) that are built up by Fe B-sites and O-sites.

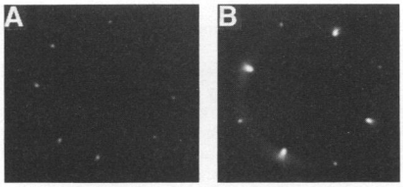

Fig. 2. LEED patterns of the mechanically polished and annealed $Fe_3O_4(001)$ surface, obtained at (**A**) 86- and (**B**) 142-eV electron energy.

highly useful tool in the study of the topographic and magnetic surface structure of magnetic materials down to the atomic level.

The most natural way to make the STM magnetic-sensitive is, of course, to replace the commonly used nonmagnetic W and PtIr tips with magnetic probe tips. However, it was only recently when the first report of STM experiments with magnetic probe tips under well-defined ultrahigh vacuum (UHV) conditions appeared (*9*). By using ferromagnetic CrO_2 tips and a Cr(001) test surface, we were able to demonstrate that vacuum tunneling of spin-polarized electrons is observable in the STM. This allowed us to distinguish the alternately magnetized terraces of the Cr(001) surface on a nanometer scale and to derive a local effective

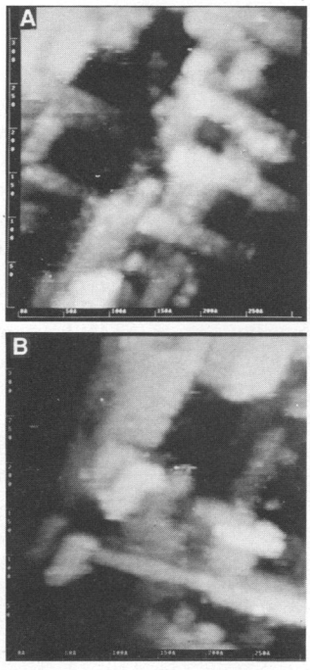

Fig. 3. STM overview images (300 Å by 300 Å) showing the first kind of topography observed at the $Fe_3O_4(001)$ surface on a nanometer scale. Different terraces that are predominantly separated by steps 4.2 Å high are visible. No characteristic difference in the STM images obtained with (**A**) a W tip and (**B**) an Fe tip is found on this length scale. (Tunneling current I = 1 nA, and sample bias voltage U = +3.0 V for both images.)

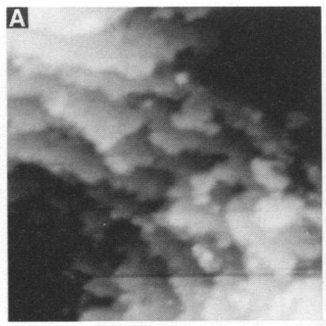

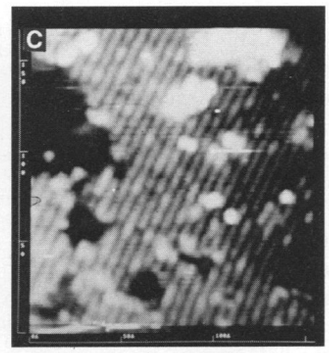

Fig. 4. (**A**) STM overview image (300 Å by 300 Å) showing the second kind of topography observed at the $Fe_3O_4(001)$ surface. Different terraces are visible that are separated by ragged steps ~2 Å high (W tip, I = 1 nA, and U = +3.0 V). (**B**) Higher-magnification STM image (150 Å by 150 Å) showing atomic rows on top of the terraces that change their orientation by 90° from one terrace to the next. The Z scale covers 2 nm (W tip, I = 1 nA, and U = +3.0 V). (**C**) STM image (150 Å by 150 Å) showing the atomic rows on a single extended terrace (Fe tip, I = 1 nA, and U = +3.0 V).

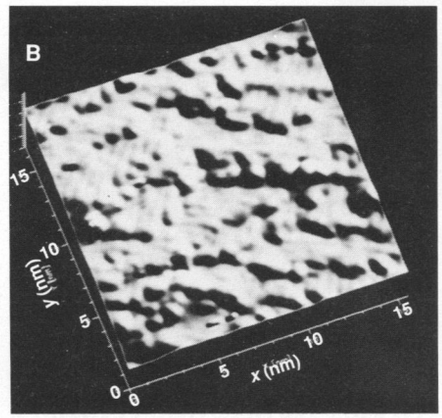

polarization of the tunnel junction (*9, 10*).

In our more recently performed STM experiments in which we used ferromagnetic Fe probe tips prepared in situ and a magnetite sample, we have aimed at coming down to the atomic level in probing the topographic and magnetic surface structure of a well-known magnetic material. Atomically sharp and clean Fe tips were obtained with an in situ tip preparation procedure as described (*11*). In this method, a polycrystalline, 0.25-mm-diameter Fe wire is electrochemically etched until a constriction 20 to 100 μm in diameter is formed. One end of the wire is then fixed in the tip holder of the STM unit, whereas the other end of the wire is fixed in another tip holder on top of a standard sample holder. The two ends are pulled apart in UHV (10^{-11} mbar) by flipping back the scan-head of the STM unit (*12*). As a result of this procedure, nanotips are formed at the foremost end of the tips, with a radius of curvature of 10 nm or even less. The cleanness of the tips at the foremost end is only limited by the bulk impurity concentration.

Natural single crystals of magnetite (Fe_3O_4) were used as samples for our STM studies. Magnetite is ferrimagnetic, with a Curie temperature of 860 K and a room-temperature conductivity of ~100 ohm^{-1} cm^{-1}. It has a cubic inverse spinel structure and the formula unit may be written as $Fe^{3+}[Fe^{2+},Fe^{3+}]O_4$ from the ionic crystal point of view. A simplified picture of the conventional unit cell of magnetite is shown in Fig. 1. The crystals were well characterized by x-ray diffraction and electrical resistivity measurements as a function of temperature. Several different methods for preparing a well-defined (001) surface of magnetite were tried. In situ cleavage of the crystals in UHV leads to clean but rough surfaces. Therefore, we used a surface preparation procedure consisting of mechanical polishing and then in situ annealing up to 1000 ± 50 K. This annealing treatment did not change the stoichiometry and atomic structure at the surface, as checked with Auger electron spectroscopy (AES), x-ray photoelectron spectroscopy (XPS), low-energy electron diffraction (LEED), and STM. The AES spectra proved that a clean magnetite surface was obtained by the annealing treatment (impurity concentration less than 1% of a monolayer, which corresponds to our detection limit). LEED patterns such as those in Fig. 2 were reproducibly obtained after surface preparation. A quantitative analysis indicated that the $Fe_3O_4(001)$ surface was nonreconstructed. The STM experiments were performed at room temperature in the same multichamber UHV system (Nanolab) that contained the surface preparation and conventional surface analysis facilities. The pressure was at least in the low 10^{-11}-mbar range, guaranteeing a reasonable surface cleanness over several hours. All of the experimental STM results below represent raw data.

We first characterized the nanotopography of the $Fe_3O_4(001)$ surface by using both electrochemically etched W tips and Fe tips prepared in situ. Two characteristic but completely different topographies were found in different surface regions. In Fig. 3, A and B, are STM images of the first kind of topography, as obtained with W and Fe tips, respectively. No characteristic difference be-

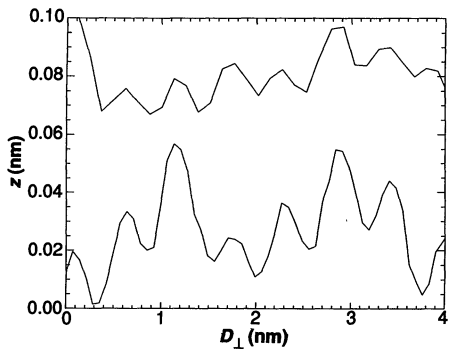

Fig. 5. Single line sections perpendicular to the atomic rows in the STM images of Fig. 4, B and C ($D\perp$, distance along xy plane). A 6 Å periodicity is observed with a W tip (top line section) as well as with an Fe tip (bottom line section).

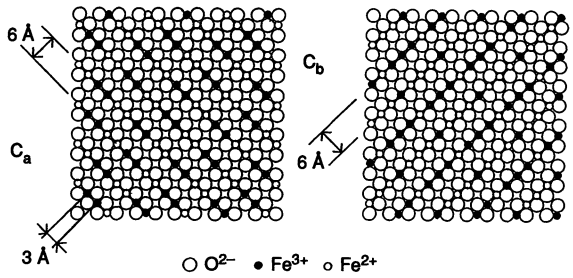

Fig. 7. Structure model for the Fe–O (C_a and C_b) planes of the low-temperature phase of $Fe_3O_4(001)$ below the order-disorder transition (*14*). A distinction between the different ionic species Fe^{2+} and Fe^{3+} has been made. The repeat period of Fe^{2+} and Fe^{3+} is four times the spacing of 3 Å between the Fe sites along the Fe rows, that is, 12 Å. This period is equal to the most frequently observed periodicity in the STM images obtained at room temperature.

tween the experimental results obtained with nonmagnetic and magnetic tips can be found on this scale of several hundred angstroms. Different terraces appear in these images that are predominantly separated by steps 4.2 Å high that correspond to one-half of the height of the conventional unit cell in Fig. 1. The right angles, which are always found, reflect the symmetry of the (001) surface of magnetite. The square holes, typically 4.2 Å deep, can be as small as 34 Å by 34 Å. Atomic resolution STM images obtained on top of the terraces (*13*) reveal a periodic square lattice, corresponding to the top (001) plane of the crystal structure in Fig. 1, which is built up by tetrahedrally coordinated Fe^{3+} A-sites.

Another kind of topography, much less frequently observed, is shown in the STM images of Fig. 4, which were also obtained with W as well as Fe probe tips. Again, terraces can be seen that, in contrast to the STM images of Fig. 3, are separated by ragged steps only 2 Å high. On top of these terraces, atomic rows that change their orientation by 90° from one terrace to the next are clear. The separation between these atomic rows is ~6 Å, as measured with

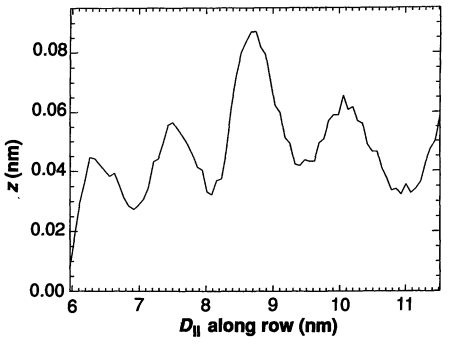

Fig. 6. Single line section along an atomic row of Fe B-sites, as measured with an Fe tip, showing the presence of a 12 Å periodicity. This line section was taken from the STM image in Fig. 4C.

both W and Fe tips (Fig. 5). By comparison with the crystal structure of magnetite (Fig. 1), we found that the STM images in Fig. 4 correspond to the Fe–O(001) crystal planes. These Fe–O planes are indeed separated by ~2 Å, and they are built up by rows of octahedrally coordinated Fe B-sites (Fe^{2+} and Fe^{3+}), which have a spacing of ~6 Å and change their orientation by 90° from one Fe–O plane to the next (Fig. 1). The rows of O sites, which are not visible in our STM images, would have a spacing of 3 Å. The fact that only the Fe rows are visible in the STM images, which were obtained with a positive sample bias, indicates the presence of a spectroscopic effect with a dominant tunneling contribution through the empty Fe $3d$ states of the $Fe_3O_4(001)$ surface.

By a comparison of the atomic resolution STM images obtained with nonmagnetic W tips and ferromagnetic Fe tips, we have found clear differences in the appearance of the Fe rows. In the STM images obtained with the nonmagnetic W tips, the rows of Fe sites always appear structureless; in other words, the measured corrugation amplitudes along the Fe rows are below 0.1 Å, equivalent to the noise level in these STM studies. The absence of a periodic corrugation along the Fe rows when measured with a nonmagnetic W tip may be explained by the small separation of 3 Å between the Fe sites along the Fe rows. By a further decrease of the noise level, it is expected that a periodic corrugation along the Fe rows with a 3 Å period could be observed with the W tip. In contrast, by using the ferromagnetic Fe probe tips, we have clearly found a significant corrugation along the Fe rows that was highly reproducible (Fig. 4C). Surprisingly, the most frequently observed period is not 3 Å, as expected for a topographic image, but 12 Å, which corresponds to four times the spacing of 3 Å between the Fe B-sites along the Fe rows (Fig. 6). An explanation for the dominance of the 12 Å periodicity can only be found by considering the different ionic species Fe^{2+} and Fe^{3+} present in Fe_3O_4. According to structure models for the low-temperature phase of magnetite below the order-disorder (Verwey) transition (*14–16*), the repeat period of Fe^{2+} and Fe^{3+} along the Fe rows should be exactly four times the 3 Å spacing between Fe sites (Fig. 7). The fact that the ferromagnetic Fe probe tip is sensitive to this repeat period proves the presence of a magnetic-contrast mechanism at the atomic level, which is based on the different spin configurations $3d^5\uparrow 3d^\downarrow$ for Fe^{2+} and $3d^5\uparrow$ for Fe^{3+}. A simplified picture for the origin of the line scan in Fig. 6 is presented in Fig. 8.

A strictly periodic corrugation with the 12 Å period is only observed on a local scale (up to ~50 Å). Other periodicities that are multiples of 3 Å are also found, which are, however, much less frequently observed than the 12 Å period. The present STM experiment was performed at room temperature, whereas the order-disorder (Verwey) transition in the bulk occurs well below room temperature (at ~120 K). The order-disorder transition temperature is likely increased at the surface of magnetite because of the reduced coordination and band-narrowing at the surface. However, long-range order is not present at room temperature, as

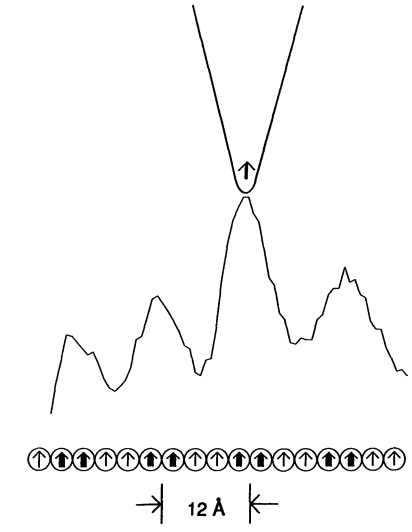

Fig. 8. Simplified picture for the origin of the measured line section in Fig. 6. The observed magnetic contrast on the atomic scale was attributed to the different spin configurations (that is, the different magnetic moments) of Fe^{2+} and Fe^{3+}

deduced from our STM study, and is not expected to be seen with experimental techniques that average over large surface areas. Our STM observations instead support a glassy state at the surface with medium-range order at room temperature.

Because a microscopic theory for STM experiments with a magnetic tip and sample is lacking, we can only speculate about the origin of the magnetic contrast observed at the atomic level. Magnetic dipole forces, although present, are not expected to lead to magnetic contrast on the atomic scale because of their long-range nature. Therefore, either spin-polarized tunneling or, less likely, the effect of magnetic exchange forces might be responsible for the observed contrast.

In summary, we have characterized the nanotopography and the atomic and magnetic surface structure of a well-known mineral by using STM with nonmagnetic as well as with magnetic sensor tips. The discovery of magnetic contrast at the atomic level allowed us to detect local order in the spatial distribution of the different magnetic ions Fe^{2+} and Fe^{3+} at the (001) surface of Fe_3O_4 at room temperature. We believe this study has proven that STM will become a most valuable tool in scientific research fields such as surface magnetism, transition metal oxides, and geology as well.

REFERENCES AND NOTES

1. G. Binnig, H. Rohrer, Ch. Gerber, E. Weibel, *Phys. Rev. Lett.* **49**, 57 (1982).
2. R. J. Hamers, *Annu. Rev. phys. Chem.* **40**, 531 (1989).
3. R. M. Feenstra, in *Scanning Tunneling Microscopy and Related Methods*, R. J. Behm, N. Garcia, H. Rohrer, Eds. (vol. 184 of *NATO ASI Series E: Applied Science*, Kluwer, Academic, Dordrecht, Holland, 1990), pp. 211–240.
4. R. J. Behm, *ibid.*, pp. 173–209.
5. H. F. Hess, R. B. Robinson, J. V. Waszczak, *Phys. B* **169**, 422 (1991).
6. R. V. Coleman *et al.*, *Adv. Phys.* **37**, 559 (1988).
7. D. M. Eigler and E. K. Schweizer, *Nature* **344**, 524 (1990).
8. D. M. Eigler, C. P. Lutz, W. E. Rudge, *ibid.* **352**, 600 (1991).
9. R. Wiesendanger, H.-J. Güntherodt, G. Güntherodt, R. J. Gambino, R. Ruf, *Phys. Rev. Lett.* **65**, 247 (1990).
10. R. Wiesendanger *et al.*, *J. Vac. Sci. Technol. B* **9**, 519 (1991).
11. R. Wiesendanger *et al.*, *Appl. Phys. A* **53**, 349 (1991).
12. R. Wiesendanger *et al.*, *Vacuum* **41**, 386 (1990).
13. R. Wiesendanger *et al.*, in preparation.
14. S. Iida *et al.*, *J. Appl. Phys.* **53**, 2164 (1982).
15. S. Iida, M. Mizoguchi, N. Goto, Y. Motomura, *J. Magn. Magn. Mater.* **31–34**, 771 (1983).
16. E. Kita, Y. Tokuyama, A. Tasaki, K. Siratori, *ibid.*, p. 787.

17. Financial support from the Swiss National Science Foundation is acknowledged.

23 September 1991; accepted 27 November 1991

Effects of High Temperature on Silicate Liquid Structure: A Multinuclear NMR Study

J. F. STEBBINS AND IAN FARNAN

The structure of a silicate liquid changes with temperature, and this substantially affects its thermodynamic and transport properties. Models used by geochemists, geophysicists, and glass scientists need to include such effects. In situ, high-temperature nuclear magnetic resonance (NMR) spectroscopy on ^{23}Na, ^{27}Al, and ^{29}Si was used to help determine the time-averaged structure of a series of alkali aluminosilicate liquids at temperatures to 1320°C. Isotropic chemical shifts for ^{29}Si increase (to higher frequencies) with increasing temperature, probably in response to intermediate-range structural changes such as the expansion of bonds between nonbridging oxygens and alkali cations. In contrast, isotropic chemical shifts for ^{27}Al decrease with increasing temperature, indicating that more significant short-range structural changes take place for aluminum, such as an increase in mean coordination number. The spectrum of a sodium aluminosilicate glass clearly indicates that at least a few percent of six-coordinated aluminum was present in the liquid at high temperature.

MOLTEN SILICATES ARE THE PRECURSORS of almost all igneous rocks (and therefore much of the earth's crust and mantle) and are the initial states of commercial glasses and glass-ceramics. Silicate melts are strongly bonded, partially ionic liquids, whose behavior is in many ways intermediate between those of organic molecular liquids and ionic molten salts (*1*). Most direct information about silicate liquid structure comes from studies of glasses, which contain configurations that are frozen in as temperature drops through the glass transition temperature T_g. However, large increases in heat capacity, thermal expansion, and compressibility on heating through T_g suggest that, above this point, significant structural changes occur with increasing temperature (*2*). Quantification of these changes is of key importance in understanding the properties of the liquids near and above their melting points, which are typically several hundred to more than 1000°C above T_g: high-temperature structure and dynamics control the properties of silicate liquids most relevant to geochemistry, geophysics, and materials science.

In situ high-temperature studies of vibrational (*3*) and x-ray absorption spectra (*4*) have indicated some details of the local structural changes that can take place with increasing temperature or on melting of silicates. Earlier work has shown that some temperature-induced liquid structural changes can be determined from NMR spectra of glass samples quenched at different rates and therefore recording different T_g values (*5, 6*). NMR has also been used to study ^{17}O, ^{23}Na, ^{27}Al, ^{29}Si, and other nuclides in silicate liquids at high temperature (*1, 7–11*). Most of this work has concentrated on the mechanism of the dynamic exchange among structural species at temperatures only a few hundred degrees above T_g. At higher temperatures, the NMR signals from all structural groups are fully averaged by rapid exchange and reorientation, even when that exchange involves breaking strong Si–O bonds (*7–10*). Recently, a systematic difference in isotropic chemical shifts for ^{27}Al between glasses and high-temperature liquids was recognized (*11*). These data suggested that changes in the average structure with temperature could be directly observed in the liquid state. From NMR data on a single nuclide, however, it has not been possible to determine the mechanism of these changes and relate them to thermodynamic properties. Some temperature effects, such as changes in bulk magnetic susceptibility, should cause similar perturbations in the NMR frequencies of different nuclides. Temperature-induced structural changes, on the other hand, could affect different nuclides similarly or dissimilarly, depending on their chemical behavior. We present here results from high-T NMR spectroscopy of ^{23}Na, ^{29}Si, and ^{27}Al that, taken together, place new constraints on the mechanism of temperature-induced structural change in silicate liquids.

We prepared a variety of alkali silicate and aluminosilicate glasses (*12*), chosen to minimize liquidus temperatures and viscosities and to allow simultaneous study of several nuclides (Table 1). In collecting the NMR data at room temperature, we used the

Department of Geology, Stanford University, Stanford, CA 94305.